Wide Range Calibration Method for Direct Interface Circuits and Application to Resistive Force Sensors

José A. Hidalgo-López, Óscar Oballe-Peinado, Julián Castellanos-Ramos, Juan C. Tejero-Calado and Fernando Vidal-Verdú

***Abstract*— A novel approach to interface resistive sensors directly to a Field Programmable Gate Array (FPGA) is presented in this paper. The circuit is based on Direct Interface Circuits (DICs), which make the sensor reading through a magnitude-to-time-to-digital conversion using just a few passive elements and a programmable digital device. Specifically, the system uses two calibration resistors of known value, two capacitors, and a new equation to estimate the sensor resistance in order to obtain an improved estimation in both the high and low parts of the resistance range. Furthermore, the new method can be used for reading resistive force sensors, with the advantage that the equations can be adapted for the output to directly provide the force exerted, thus avoiding the need for a resistance-to-force conversion. The circuit has been implemented using an FPGA as the programmable digital device to characterize the system, which allows both the reading of discrete resistors and those of a commercial force sensor. When discrete resistors are measured, estimation error in the low part of the range (a few hundred ohms) is reduced between twofold and fivefold compared to the results provided by other DICs. Moreover, the most significant errors produced by the new method when reading a force sensor come in the high part of the range (several tens of Newtons), standing at just 0.88%, compared to errors between 1.94% and 5.23% of other methods proposed in the literature.**

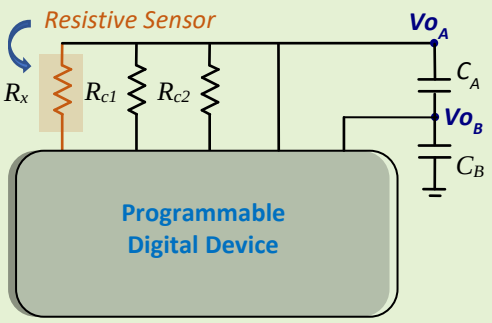

***Index Terms*— Direct interface circuits, interface sensor, resistive sensor, time-based measurement.**

I. Introduction

A lot of tactile sensors are based on piezoresistive principles, meaning conductance between the two electrodes of each sensing unit (taxel) depends on the applied force. Some of these sensors consist basically of a layer of sensitive material placed between electrodes. This material changes the contact area at a microscopic scale due to roughness at the contact interface [1]–[3]. This operation principle results in very thin sensors, some of which are commercially available [4]–[6].

Several analytical models quantify the relationship between the force applied in this kind of sensor and their conductance [7]–[10], some of them based on tribology [11]. All these models obtain a linear relationship between the total normal force on the sensor and the resulting electrical conductance between the electrodes over a wide range of loads. Therefore, under this assumption, we can write:

$$F_x = \frac{\alpha}{R_x} \tag{1}$$

where R_x is the resistance measured between the sensor's electrodes, F_x is the force applied, and α is a constant that depends on the electrical and mechanical properties of the materials between the electrodes [12]. Thus, according to (1), F_x can be estimated with an electronic circuit that measures R_x while knowing the value of α. Additionally, F_x is converted to digital format to process the force information through Programmable Digital Devices (PDDs).

One approach to obtain F_x as a digital output is to use a simple conditioning circuit (CC) with a voltage source and a known resistor forming a voltage divider with R_x. This solution provides a voltage that depends on R_x, which can be fed to an analog-to-digital converter (ADC) to obtain the digital output. The problem with this circuit is that the relationship between digital output and force is not simple, and further processing is required to obtain the value of F_x. This can be avoided by using an inverting operational amplifier as the CC since the circuit's output voltage is inversely proportional to R_x (and, therefore, directly proportional to F_x). Except for a scale factor, the ADC output provides the force exerted on the sensor as a digital output. However, ADCs are needed in both solutions and operational amplifiers (OAs) in the second case.

Another approach for reading sensors is to perform a resistance-to-frequency conversion (or capacitance-to-frequency, which is very common in capacitive sensors). In

Sent July 13, 2021. This work was supported by the Spanish Government and by the European ERDF program funds under Contract TEC2015-67642-R (*Corresponding author: José A. Hidalgo-López*).

J. A. Hidalgo-López, Ó. Oballe-Peinado, J. Castellanos-Ramos, J. C. Tejero-Calado, and F. Vidal-Verdú are with the Departamento de Electrónica, Universidad de Málaga, Málaga 29071, Spain, and also with the Instituto de Investigación Biomédica de Málaga (e-mail: jahidalgo@uma.es; oballe@uma.es; jcramos@uma.es; jctejero@uma.es; fvidal@uma.es).

these circuits, the output signal is a type of periodic waveform that oscillates between the logic levels of a PDD. When the signal is taken to the PDD, this device measures the time (in clock cycles) in which the input signal is interpreted as a constant logic value. A simple counter allows a period-to-digital conversion. A large number of circuits perform this type of conversion [13]–[20]. Apart from a set of passive elements, all these implementations involve a variable number of OAs and, in some cases, analog switches.

The two methodologies indicated above can be very expensive or even impossible to implement if the intention is to perform the reading of multiple taxels, e.g., in an electronic skin [21] or systems for Seat Occupancy Detection [22]. The hardware needed to generate the digital output of the sensor reading must be as simple as possible. Furthermore, in the case of many taxels, the digital processing of their information may require a certain degree of parallelism. This is the reason why FPGAs are used as PDDs, given their versatility and parallel processing capabilities. However, FPGAs do not usually incorporate ADCs. This means that the designer must integrate multiple ADCs and OAs into the design, making it expensive in terms of hardware, size, power consumption, and price.

In contrast to these implementations are the so-called Direct Interface Circuits (DICs), which perform the estimation of R_x by means of a resistance-to-time-to-digital conversion [23]–[27], without the need for ADCs, OAs, or analog switches. DICs are a straightforward option since, in addition to R_x, they only require some calibration resistors, a capacitor, and a PDD to carry out time-based measurements which determine the resistance R_x. Using an FPGA to perform these time-based measurements allows many resistive sensors to be read simultaneously in a straightforward manner. Moreover, the same operating principle can be applied to capacitive or inductive sensors [28]–[32].

However, three problems limit the use of DICs in resistive sensors. The first issue is the importance of quantization errors in the measurement of times for low resistances. If quantization errors are not reduced, sensors with resistance ranges of a few hundred ohms could not use DICs for their measurement. For example, Resistance-Temperature-Detectors (RTD) commonly have a nominal resistance in the 100 Ω - 1 kΩ range, or porous silicon gas sensors for HCl, NO, or NH_3 concentration measurements show resistances in the 70 Ω - 160 Ω range. Second is the high degree of uncertainty in the time measurements for high resistance values, from several kΩ onwards, due to the presence of noise in the circuit. Although there have been proposals to reduce the impact of both issues [33], [34], it has hitherto proven impossible to carry out these improvements simultaneously with a single circuit. The third issue is related to the magnitude measured by the sensor: a DIC provides the digital value of R_x, not of the magnitude of the applied force. Hence, obtaining F_x in the force sensor requires using (1) to perform the R_x to F_x conversion. In turn, this requires time and possibly additional hardware to perform the calculations and the storage of parameter α.

Unfortunately, a tactile sensor can have resistances in a wide range, from a few hundred ohms to several tens of kΩ, and, in addition, it requires a complex measurement process to obtain α.

To solve these issues, this paper presents a new estimation method based on the DIC structure proposed in [34] that simultaneously reduces errors in the calculation of high and low resistances. Furthermore, the new method can be modified so that F_x is estimated directly, thus avoiding a calibration process to obtain the parameter α. As the results are obtained in terms of forces and not resistances, savings are achieved in characterization measures, computation time, storage, and hardware requirements.

The structure of the paper is as follows. Section 2 presents the operating principles of DICs found in the literature. Section 3 sets out the new proposed DIC, including a quantitative analysis of its operation. Section 4 provides an overview of the materials and methods used in evaluating the new DIC. Section 5 presents and discusses the experimental results. Finally, Section 6 sets out the conclusions of this paper.

II. Operating Principle

The DIC for measuring resistive sensors most commonly cited in the literature is the so-called Two-Point Calibration Method (TPCM), as shown in Fig. 1(a) (it is important to note that, although FPGAs are used in all circuits in Fig. 1, these can be replaced by any other PDD). TPCM is used due to the fact that it presents smaller errors in estimating R_x than other simpler methods. For the estimation of R_x, the circuit in Fig. 1(a) performs three processes of charging and discharging the capacitor, C. Each charging process precedes a discharging process, always carried out in the same way: configuring pins Pp, Pc1, Pc2, and Px of the FPGA in Fig. 1(a) as outputs and establishing a logic 1 output in them. Therefore, the capacitor is charged to the maximum voltage allowed by these pins, usually the buffer voltage supply of the FPGA, V_{DD}. The R_p resistor is optional, although it is used to decrease the noise that can appear in the voltage value stored in C at the end of the charging process [35]. Discharging of C is carried out at the end of each charging process, using a different resistor each time: either of the two calibration resistors of known value, R_{c1} or R_{c2}, ($R_{c2} > R_{c1}$), or of R_x. These discharge processes are performed by configuring the pin connected to the resistor through which discharge is carried out as a logic 0 output. Meanwhile, the rest of the FPGA pins will be configured in high impedance state, HZ, in order not to alter the capacitor discharge. The discharge ends when voltage V_{Th} is reached in C, called the trigger instant. V_{Th} is the threshold voltage for the detection of a logic 0 input in an FPGA pin. Therefore, three measurements of discharging times T_x, T_{c1}, and T_{c2} corresponding to each of the resistors are obtained. These measurements take the form

$$T = (R + Ro) \cdot C \cdot \ln\left(\frac{V_{DD}}{V_{Th}}\right) \tag{2}$$

where Ro is the output resistance of the FPGA buffer (internal output resistance in series with the output voltage of the buffer), and R is any resistor through which discharge is taking place. It is important to note that T will be quantized in FPGA

clock cycles.

Using (2) for T_x, T_{c1}, and T_{c2}, it is easy to find that R_x can be expressed as:

$$R_x = \frac{T_x - T_{c1}}{T_{c2} - T_{c1}} \cdot \left(R_{c2} - R_{c1}\right) + R_{c1} \tag{3}$$

The major advantage of (3) is that R_x depends on three time measurements, along with the values of R_{c1} and R_{c2}. Hence, we do not need to know *Ro*, V_{DD}, V_{Th}, or *C* to obtain R_x, as would be necessary using (2). These values can be difficult to find accurately and may also vary over time.

TPCM has two main sources of error. The first comes from uncertainty in the time measurement due to time quantization, $u_q(T)$, since T_x, T_{c1}, and T_{c2} are measured in FPGA clock cycles (T_{clk} is the period of this clock). Given that, in our system, the quantization error is at most one clock cycle and, since the error probability density function (PDF) is assumed to be a rectangular density function (the trigger instant is equiprobable at any moment of the last cycle), the value of the quantization uncertainty is constant for any time measurement. According to [36] its value is:

$$u_q(T) = \frac{T_{clk}}{\sqrt{12}} \tag{4}$$

In consequence, considering (2), the relative value of this uncertainty, $u_q(T)/T$, decreases as *R* and *T* increase:

$$\frac{u_q(T)}{T} = \frac{1}{\sqrt{12}} \frac{T_{clk}}{T} = \frac{1}{\sqrt{12}} \frac{T_{clk}}{(R + Ro) \cdot C \cdot \ln\left(\frac{V_{DD}}{V_{Th}}\right)} \tag{5}$$

This equation provides two ways to decrease $u_q(T)/T$. The first is to increase clock frequency, although this is not always possible due to limitations in the FPGA itself or in the power consumption of the system. The other possible solution is to increase *C*, which, according to (2), leads to an increase of *T*, but this slows down the estimation of R_x.

The second source of error in TPCM comes from uncertainty in detecting the trigger instant. This uncertainty, known as trigger uncertainty, $u_{trigger}(T)$, is inversely proportional to the slope of the discharge curve through *R* at the instant when *Vo* in Fig. 1(a) reaches V_{Th} [36]. As *Vo* is

$$Vo(t) = V_{DD} \cdot e^{-t/(R+Ro)\cdot C} \tag{6}$$

then $u_{trigger}(T)$ is given by

$$u_{trigger}(T) = \frac{k}{\left|\frac{dVo}{dt}\right|_{t=T}} = \frac{k \cdot \left(R + Ro\right) \cdot C}{V_{Th}} \tag{7}$$

This equation shows that trigger uncertainty increases with higher values of *R*. The value of $u_{trigger}$ can be reduced by decreasing *k* (parameter associated with electrical noise in the circuit) in (7) through careful circuit design. However, beyond this, TPCM cannot diminish the relative value of this uncertainty since:

$$\frac{u_{trigger}(T)}{T} = \frac{k}{V_{Th} \cdot \ln\left(\frac{V_{DD}}{V_{Th}}\right)} \tag{8}$$

The results of (5) and (8) show that, as *R* increases $u_q(T)/T$ decreases, however according to (8), $u_{trigger}(T)/T$ is independent of *R*, so it becomes the dominant term for medium-high resistances, as it is shown by the experimental results in [36].

To reduce the effect of quantization without reducing estimation speed or increasing the clock frequency, [33] proposes the DIC shown in Fig. 1(b) and an equation other than (3) to estimate R_x. This method, known as Quantization Error Reduction Method (QERM), also has three charging and discharging processes. The charging processes and the discharging process through R_{c1} are the same as for TPCM. However, in this circuit $R_{c1} + R_{c2}$ plays the role of the second calibration resistor since it is the equivalent resistor through which discharge takes place when configuring the Pc2 pin as a logic 0 output. The third discharge process is performed by configuring pins Px and Pc2 as a logic 0 output (meaning discharge is performed through R_x and $R_{c1} + R_{c2}$ simultaneously), while Pc1 and Pp are configured as inputs (HZ). This pin configuration makes it possible to detect when voltages $Vo(t)$ and $Vo_C(t)$ of Fig. 1(b) reach V_{Th}. The key idea in the QEMR is that V_{Th} is reached earlier in the Pc1 node than in Pp during this discharge due to the voltage divider formed by R_{c1} and R_{c2}. Thus, if the time that elapses until $Vo_C = V_{Th}$ is below a certain amount, discharge is carried out through a small resistor and, from this moment on, continues solely through Pc2 until $Vo(t)$ reaches V_{Th}. This reduces quantization error since $R_{c1} + R_{c2}$ is in the high part of the range. The only drawbacks of QERM are that pin control is somewhat more complicated than in TPCM, and that the estimation equation (obtained in [33]) is also more complex compared to (3).

QERM reduces uncertainty in the low resistance range, although a different circuit is required to decrease trigger uncertainty [34]. This is known as the Two-Capacitor Direct Interface Circuit (TCDIC). As shown in Fig. 1(c), this circuit involves a simple modification of TPCM by including a second capacitor and a new trigger instant detection pin. Pins P_A and P_B in Fig. 1(c) detect when voltages $Vo_A(t)$ and $Vo_B(t)$ of nodes A and B of capacitors C_A and C_B reach voltage V_{Th}. Three charging and discharging processes are again carried out in order to determine R_x. In each charging process, all pins are also configured as a logic 1 output, such that C_B is charged at V_{DD}, while C_A is actually fully discharged. After each charging process, discharges are made through each of the resistors R_x, R_{c1} or R_{c2}, as in TPCM. The only difference in the discharges with respect to TPCM is that two time measurements are made in each discharge: T_A for the instant when $Vo_A = V_{Th}$, and T_B for the instant when $Vo_B = V_{Th}$. Voltages Vo_A and Vo_B are given by [34]

This article has been accepted for publication in IEEE Sensors Journal. This is the author's version which has not been fully edited and content may change prior to final publication. Citation information: DOI 10.1109/JSEN.2021.3107589

$$Vo_A(t) = V_{DD} \cdot e^{-t/(R+Ro)\cdot C_T}$$
$$Vo_B(t) = Vo_A(t) \cdot \frac{C_A}{C_A + C_B} + V_{DD} \cdot \frac{C_B}{C_A + C_B} \quad (9)$$

where $C_T = C_A \parallel C_B$. From these equations, it is found that T_A and T_B are respectively:

$$T_A = (R + Ro) \cdot C_T \cdot \ln\left(\frac{V_{DD}}{V_{Th}}\right)$$
$$T_B = (R + Ro) \cdot C_T \cdot \ln\left(\frac{V_{DD} \cdot C_A}{V_{Th} \cdot (C_A + C_B) - V_{DD} \cdot C_B}\right) \quad (10)$$

Thus, times T_{xA} and T_{xB} are obtained in the discharge through R_x, and T_{c1A}, T_{c1B}, T_{c2A}, and T_{c2B} in the discharges through the calibration resistors. These six times can be used to estimate R_x using [34]:

$$R_x = \frac{T_{xA} + T_{xB} - (T_{c1A} + T_{c1B})}{T_{c2A} + T_{c2B} - (T_{c1A} + T_{c1B})} \cdot (R_{c2} - R_{c1}) + R_{c1} \quad (11)$$

The advantage of this equation over (3) is that when choosing capacitors with $C_A >> C_B$, uncertainty in the R_x measurement using the TCDIC, $u(R_x)_{TCDIC}$, is smaller than that obtained using TPCM, $u(R_x)_{TPCM}$. It is important to note that in (3) and (11) uncertainties in the estimate of R_x come from the uncertainties in the time measurements used for its calculation. In particular, for medium-high resistance values, where the effect of quantization is negligible, and errors in the estimations are mainly due to trigger uncertainty, it can be proved that [34]:

$$u(R_x)_{TCDIC} \approx \frac{1}{\sqrt{2}} u(R_x)_{TPCM} \quad (12)$$

QERM and TCDIC reduce errors in estimating R_x when compared with those obtained by the TPCM. However, each one does so in a particular part of the range, so it is impossible to reduce TPCM errors for both high and low resistance values with a single circuit. To combine the benefits of QERM and TCDIC using a single circuit, we present a new method of estimating R_x, based on the TCDIC, which simultaneously reduces errors over the entire range without any additional hardware. We call this method the Compact Error Reduction Method (CERM).

III. Compact Error Reduction Method

CERM uses the same circuit as TCDIC and, therefore equation (11), as the basis for the estimation of R_x. It also requires the same three charging and discharging processes and six time measurements. CERM achieves the same reduction of uncertainty in estimating resistances in the medium-high part of the range. The only difference between the two methods comes in the final part of the discharge that starts through R_x whenever its value is low. As will be shown below, this modification aims to obtain a more accurate estimation of T_{xA} and T_{xB} for low resistances. Fig. 2 indicates the waveforms for the pins of the PDD in the CERM circuit and the voltages Vo_A and Vo_B for the two possible situations: on the left side, when R_x has medium-high values and, on the right side, when R_x has low values. In the second case, the last discharge starts through R_x and ends with R_{c2}.

Fig. 3 shows, in detail, the new discharge where, initially, all the pins of the circuit in Fig. 1(c) are configured as HZ except Px, which is configured as a logic 0 output. During the first part of the discharge, Vo_A is given by the first equation in (9), replacing R with R_x. If R_x is small, the time constant in this equation is small, and there are significant variations in Vo_A in a clock cycle. Fig. 3 shows how this can cause voltage $Vo_A(T_{xA})$ to be significantly lower than V_{Th} at the end of the cycle in which the trigger instant is detected (Fig. 3 shows this effect highly amplified for clarification). The same can occur with $Vo_B(T_{xB})$ if the discharge continue through R_x once T_{xA} is reached, as in the case of the TCDIC. This is an alternative way of understanding the increasing effects of quantization as R_x decreases.

As shown in Figs. 2 and 3, in CERM for low resistances, once T_{xA} is reached, discharge continues through Rc_2 until $Vo_B = V_{Th}$. Thus, more accurate inferred measurements of the trigger instant in nodes A and B are obtained, which we call Ti_{xA} and Ti_{xB}. The time from T_{xA} to $Vo_B = V_{Th}$ is $T_{c2,x}$ in Fig. 3. Since R_{c2} is a resistor in the high part of the range, $T_{c2,x}$ is a good estimation of the time it takes Vo_B to go from $Vo_B(T_{xA})$ to V_{Th} (error due to quantization in this time is negligible). The critical fact is that more precise measurements can be inferred from the instants at which Vo_A and Vo_B reach V_{Th} using the two measured times, T_{xA} and $T_{c2,x}$. To find Ti_{xA}, T_{xA} and Ti_{xA} are written using (2)

$$T_{xA} = (R_x + Ro) \cdot C_T \cdot \ln\left(\frac{V_{DD}}{Vo_A(T_{xA})}\right)$$
$$Ti_{xA} = (R_x + Ro) \cdot C_T \cdot \ln\left(\frac{V_{DD}}{V_{Th}}\right) \quad (13)$$

$Vo_A(T_{xA})$ is the value of Vo_A when discharging through R_x for time T_{xA} (see Fig. 3). The equation (13) can be used to find the quotient between T_{xA} and Ti_{xA} as

$$\frac{Ti_{xA}}{T_{xA}} = \frac{(R_x + Ro) \cdot C_T \cdot \ln\left(\frac{V_{DD}}{V_{Th}}\right)}{(R_x + Ro) \cdot C_T \cdot \ln\left(\frac{V_{DD}}{Vo_A(T_{xA})}\right)} = \frac{\ln\left(\frac{V_{DD}}{V_{Th}}\right)}{\left[\ln\left(\frac{V_{DD}}{Vo_A(T_{c2B})}\right) - \ln\left(\frac{Vo_A(T_{xA})}{Vo_A(T_{c2B})}\right)\right]} \quad (14)$$

where $Vo_A(T_{c2B})$ is the voltage reached by Vo_A during the discharge carried out only through R_{c2} when $Vo_B = V_{Th}$ ($Vo_B(T_{c2B}) = V_{Th}$).

This article has been accepted for publication in IEEE Sensors Journal. This is the author's version which has not been fully edited and content may change prior to final publication. Citation information: DOI 10.1109/JSEN.2021.3107589

Nevertheless (14) needs some modification to become a useful equation. With this objective, we define $Vo_A(T_{xA}+T_{c2,x})$ and $Vo_B(T_{xA}+T_{c2,x})$ as the voltages reached by Vo_A and Vo_B when discharging through R_x during time T_{xA} and continuing through R_{c2} during time $T_{c2,x}$ (situation in Fig. 3). Since $Vo_B(T_{c2B}) = Vo_B(T_{xA}+T_{c2,x}) = V_{Th}$, and considering that each value of Vo_B according to (9) corresponds to a single value of Vo_A, then $Vo_A(T_{xA}+T_{c2,x}) = Vo_A(T_{c2B})$ regardless of the resistors R_x the discharges are made through. With this, from (14), we can write:

$$\frac{Ti_{xA}}{T_{xA}} = \frac{(R_{c2}+Ro)\cdot C_T \cdot \ln\left(\frac{V_{DD}}{V_{Th}}\right)}{(R_{c2}+Ro)\cdot C_T \cdot \left[\ln\left(\frac{V_{DD}}{Vo_A(T_{c2B})}\right) - \ln\left(\frac{Vo_A(T_{xA})}{Vo_A(T_{xA}+T_{c2,x})}\right)\right]} = \frac{T_{c2A}}{T_{c2B}-T_{c2,x}} \quad (15)$$

Or equivalently:

$$Ti_{xA} = \frac{T_{xA}\cdot T_{c2A}}{T_{c2B}-T_{c2,x}} \quad (16)$$

Moreover, the inferred measurement Ti_{xB} can be obtained by simply observing that, from (10):

$$\frac{Ti_{xB}}{Ti_{xA}} = \frac{T_{c2B}}{T_{c2A}} \quad (17)$$

With this result and the one shown in (16) we find:

$$Ti_{xB} = \frac{T_{xA}\cdot T_{c2B}}{T_{c2B}-T_{c2,x}} \quad (18)$$

Hence, by replacing T_{xA} and T_{xB} with Ti_{xA} and Ti_{xB} in equation (11) a better estimation is obtained for R_x in the case of low resistances than with the TCDIC. The designer can simply decide which range of R_x values to make these replacements in. All required is to set a time limit, T_L, such that discharge continues through R_{c2} whenever $T_{xA} < T_L$. In this case, the above replacements are carried out in (11)

It can be concluded that the equations that describe the operation of CERM are given by:

$$R_x = \begin{cases} \dfrac{Ti_{xA}+Ti_{xB}-(T_{c1A}+T_{c1B})}{T_{c2A}+T_{c2B}-(T_{c1A}+T_{c1B})}\cdot(R_{c2}-R_{c1})+R_{c1}; T_{xA} < T_L \\ \dfrac{T_{xA}+T_{xB}-(T_{c1A}+T_{c1B})}{T_{c2A}+T_{c2B}-(T_{c1A}+T_{c1B})}\cdot(R_{c2}-R_{c1})+R_{c1}; T_{xA} \geq T_L \end{cases} \quad (19)$$

Therefore, CERM is made up of equation (19) and the circuit of Fig. 1(c).

This could raise the question as to why not use Ti_{xA} and Ti_{xB} over the entire resistance range, such that CERM would only use the equation with the condition $T_{xA} < T_L$ in (19). The answer is that uncertainty in the estimations of Ti_{xA} and Ti_{xB} obtained through the expressions (16) and (18) increases more rapidly with R_x than uncertainty in the measurements of T_{xA} and T_{xB}, and there is a value of R_x as of which T_{xA} and T_{xB} are better estimations of the trigger instants. It is important to note that uncertainties $u(Ti_{xA})$ and $u(Ti_{xB})$ appear due to the uncertainties in the measurement of the times of the terms on the right of equations (16) and (18): T_{c2A}, T_{c2B}, and $T_{c2,x}$. As in all these times, $u_{trigger}$ is much greater than u_q, $u(Ti_{xA})$ and $u(Ti_{xB})$ are mainly due to trigger uncertainties.

To check this, let us find the relative uncertainty $u(Ti_{xA})/Ti_{xA}$ using (16), the law of propagation of uncertainty, and the fact that $u(T_{c2A}) = u(T_{c2B}) = u(T_{c2,x})$ (since trigger occurs in all three time measurements when discharge is performed through R_{c2}). Hence:

$$u^2(Ti_{xA}) = \left[\left(\frac{\partial Ti_{xA}}{\partial T_{c2A}}\right)^2 + \left(\frac{\partial Ti_{xA}}{\partial T_{c2B}}\right)^2 + \left(\frac{\partial Ti_{xA}}{\partial T_{c2,x}}\right)^2\right] u^2(T_{c2A}) \quad (20)$$

It is important to note that possible uncertainty in T_{xA} is included in that of $T_{c2,x}$, since we can obtain different values of T_{xA} in different discharges through R_x, although this only modifies the instant at which discharge starts through R_{c2}. Evaluating the partial derivatives obtains:

$$\frac{u(Ti_{xA})}{Ti_{xA}} = \sqrt{\frac{1}{{T_{c2A}}^2} + \frac{2}{(T_{c2B}-T_{c2,x})^2}}\, u(T_{c2A}) \approx \sqrt{3}\cdot\frac{u(T_{c2A})}{T_{c2A}} \quad (21)$$

The approximation used is valid as long as $C_A >> C_B$, since in this case T_{c2A} and T_{c2B} are very similar, meaning $T_{c2,x} << T_{c2B}$. In any case, condition $C_A >> C_B$ must be met to verify (12) to obtain the maximum reduction of trigger uncertainty in the CERM and the TCDIC.

Following a similar procedure to obtain $u(Ti_{xB})$ we find

$$u^2(Ti_{xB}) = {Ti_{xB}}^2\left[\left(\frac{T_{c2,x}}{T_{c2B}(T_{c2B}-T_{c2,x})}\right)^2 u^2(T_{c2B}) + \frac{1}{(T_{c2B}-T_{c2,x})^2}u^2(T_{c2,x})\right] = {Ti_{xB}}^2\left[\left(\frac{T_{c2,x}}{T_{c2B}(T_{c2B}-T_{c2,x})}\right)^2 + \frac{1}{(T_{c2B}-T_{c2,x})^2}\right]u^2(T_{c2A}) \quad (22)$$

and, under the same condition that allows approximation in (21), from (22) we can write:

$$\frac{u(Ti_{xB})}{Ti_{xB}} \approx \frac{u(T_{c2A})}{T_{c2A}} \quad (23)$$

Equations (21) and (23) show that, following the discharge process of Fig. 3, the relative uncertainties in the measurement of Ti_{xA} and Ti_{xB} are constant and equal to the relative uncertainties for medium-high resistances in the case

This article has been accepted for publication in IEEE Sensors Journal. This is the author's version which has not been fully edited and
content may change prior to final publication. Citation information: DOI 10.1109/JSEN.2021.3107589

of Ti_{xB}, or multiplied by $\sqrt{3}$ in the case of Ti_{xA}. This means that, in the case of medium-high resistances, the uncertainty of the term $Ti_{xA} + Ti_{xB}$ for condition $T_{xA} < T_L$ in (19) will always be greater than that of term $T_{xA} + T_{xB}$ for condition $T_{xA} \geq T_L$. Moreover, as R_x increases, it is no longer possible to use the approximations that have allowed us to obtain (21) and (23) given that $T_{c2,x}$ increases. This leads to a rise in $u(Ti_{xA})/ Ti_{xA}$ and $u(Ti_{xB})/ Ti_{xB}$, whose values are no longer constant. Therefore, it is necessary to establish a time, T_L, that limits the maximum value of R_x using (16) and (18).

As shown, for condition $T_{xA} < T_L$, (19) provides a better estimation for low values of R_x than (11), and also improves the estimation of TPCM in the same values. This can be seen by simply observing that relative uncertainties in the $Ti_{xA} + Ti_{xB}$, $T_{c1A} + T_{c1B}$ and $T_{c2A} + T_{c2B}$ measurements in CERM, $u_{CERM}(Ti_{xA} + Ti_{xB})$, $u_{CERM}(T_{c1A} + T_{c1B})$, and $u_{CERM}(T_{c2A} + T_{c2B})$, are smaller than those of T_x, T_{c1}, and T_{c2} in TPCM, $u_{TPCM}(T_x)$, $u_{TPCM}(T_{c1})$, and $u_{TPCM}(T_{c2})$, if time constants in both circuits are equal ($C_T = C$). For $T_{c1A} + T_{c1B}$ we can write

$$\frac{u_{CERM}\left(T_{c1A}+T_{c1B}\right)}{T_{c1A}+T_{c1B}} = \frac{\sqrt{u_{CERM}^2\left(T_{c1A}\right)+u_{CERM}^2\left(T_{c1B}\right)}}{T_{c1A}+T_{c1B}} \approx \frac{\sqrt{2}\cdot u_{CERM}\left(T_{c1A}\right)}{2\cdot T_{c1A}} = \frac{u_{CERM}\left(T_{c1A}\right)}{\sqrt{2}\cdot T_{c1A}} < \frac{u_{TPCM}\left(T_{c1}\right)}{T_{c1}} \quad (24)$$

and the same applies to the measurements of R_{c2}. Moreover, from (21) and (23)

$$\frac{u_{CERM}\left(Ti_{xA}+Ti_{xB}\right)}{Ti_{xA}+Ti_{xB}} = \frac{\sqrt{u_{CERM}^2\left(Ti_{xA}\right)+u_{CERM}^2\left(Ti_{xB}\right)}}{Ti_{xA}+Ti_{xB}} \approx \frac{\sqrt{3\cdot\left(\frac{Ti_{xA}}{T_{c2A}}u_{CERM}\left(T_{c2A}\right)\right)^2+\left(\frac{Ti_{xB}}{T_{c2A}}u_{CERM}\left(T_{c2A}\right)\right)^2}}{2\cdot Ti_{xA}} \approx \frac{u_{CERM}\left(T_{c2A}\right)}{T_{c2A}} \ll \left.\frac{u_{TPCM}\left(T_x\right)}{T_x}\right|_{R_x\downarrow} \quad (25)$$

where the last term on the right in (25) is the relative uncertainty in TPCM for low resistances (mainly due to quantization). As the sums of times $Ti_{xA} + Ti_{xB}$, $T_{c1A} + T_{c1B}$, and $T_{c2A} + T_{c2B}$ are arranged as T_x, T_{c1}, and T_{c2} in the TPCM equation and have smaller relative uncertainties than those of the latter, the estimation of R_x through the first equation of (19) has a smaller uncertainty than (3). Hence, CERM outperforms TPCM when estimating any value of R_x. In contrast, it is obvious that the CERM equations present greater arithmetic complexity than for TPCM or TCDIC, in addition to needing to store a new parameter, T_L, for comparison. However, this is not really a problem with the current computational capabilities of FPGAs.

A. CERM in the Readout of Piezoresistive Force Sensors

As CERM improves estimations in the reading of resistance values with respect to TPCM and the TCDIC, it is a better alternative for the reading of any resistive sensor. Furthermore, in piezoresistive force sensors, the use of CERM is particularly suitable thanks to the relative reduction of error in the reading of low resistance values, which leads to better detection of high forces.

Using the expressions in (19), the process to obtain the force exerted on the sensor would consist of carrying out the three charging and discharging processes to find the different measurements and, from there, obtain R_x. Next, once the sensor has been characterized (or, in other words, parameter α of (1) is known), this same equation is used to find the value of F_x. However, this is both arithmetically and temporally inefficient since performing this process requires three constants to be stored in the FPGA, namely R_{c1}, R_{c2} - R_{c1}, and α, while the result of (19) must be entered in the denominator of (1), meaning an additional division is necessary.

However, it is a better option to apply known forces F_{c1} and F_{c2} to the sensor resulting in resistances of R_{c1} and R_{c2}. Thus, the first equation in (19) can be written as

$$\frac{Ti_{xA}+Ti_{xB}-\left(T_{c1A}+T_{c1B}\right)}{T_{c2A}+T_{c2B}-\left(T_{c1A}+T_{c1B}\right)} = \frac{R_x-R_{c1}}{R_{c2}-R_{c1}} = \frac{\frac{\alpha}{F_x}-\frac{\alpha}{F_{c1}}}{\frac{\alpha}{F_{c2}}-\frac{\alpha}{F_{c1}}} = \frac{\frac{1}{F_x}-\frac{1}{F_{c1}}}{\frac{1}{F_{c2}}-\frac{1}{F_{c1}}} \quad (26)$$

from which we obtain F_x. The same process can be repeated with the second equation of (19), to finally obtain the CERM equation applied to a piezoresistive force sensor:

$$F_x = \begin{cases} \dfrac{T_{c2A}+T_{c2B}-\left(T_{c1A}+T_{c1B}\right)}{\frac{1}{F_{c2}}\left[Ti_{xA}+Ti_{xB}-\left(T_{c1A}+T_{c1B}\right)\right]-\frac{1}{F_{c1}}\left[Ti_{xA}+Ti_{xB}-\left(T_{c2A}+T_{c2B}\right)\right]}; T_{xA} < T_L \\ \dfrac{T_{c2A}+T_{c2B}-\left(T_{c1A}+T_{c1B}\right)}{\frac{1}{F_{c2}}\left[T_{xA}+T_{xB}-\left(T_{c1A}+T_{c1B}\right)\right]-\frac{1}{F_{c1}}\left[T_{xA}+T_{xB}-\left(T_{c2A}+T_{c2B}\right)\right]}; T_{xA} \geq T_L \end{cases} \quad (27)$$

To evaluate F_x using (27), instead of storing R_{c1}, R_{c2}, and α, only $1/F_{c1}$ and $1/F_{c2}$ are stored. Moreover, two divisions are needed to obtain F_x from (19) and (1), while only one division is needed using (27) (divisions being the most time/hardware consuming operations).

IV. Materials and Methods

To evaluate the performance of CERM when used for a discrete resistor or a piezoresistive force sensor readout, a prototype of the circuit in Fig. 1(c) was implemented using a Spartan 6 FPGA (XC6SLX25-3FTG256) [37] from Xilinx (San Jose, CA, USA) running at 50 MHz. The prototype was manufactured with FR-4 fiberglass reinforced epoxy-

laminated substrate with four layers of conductive pathways. The internal layers were used for the supply planes, and the external layers were used for the remaining signals. Both the discrete resistors and the force sensor can be connected in the position indicated for the sensor in Fig. 1(c). The prototype is designed to evaluate the results of TPCM, TCDIC, and CERM. Three polypropylene film capacitors are used for this purpose: one of 20 nF for readout using TPCM, and two of 330 nF and 22 nF for C_A and C_B, respectively, when evaluating the performance of the TCDIC or CERM. With these values, C_T = 20.6 nF, and, therefore, the time constants in the three methods are practically the same. A set of 28 resistors ranging from 100 Ω to 16.2 kΩ has also been used to evaluate the three methods. Two calibration resistors located at approximately 15% and 85% of the range have been used, namely R_{c1} = 2320 Ω and R_{c2} = 12,700 Ω. All the resistors were measured using an Agilent 34401A digital multimeter. Five hundred measurement cycles were carried out for all resistors and all methods. The resistor under test, R_x, and the two calibration resistors are measured in each cycle. These measurements have been used to measure both errors and uncertainties in order to compare the performance of the three methods.

The piezoresistive force sensor used (replacing the discrete resistors indicated above) is the FSR 402 model from Interlink Electronics (Irvine, CA, USA) [4]. This is a low-cost sensor that has been used in multiple applications in the literature, for example, in [38]. The sensor is made up of a series of overlapping sheets. A layer of electrodes arranged in the form of a comb is superimposed on a layer of conductive material separated by an insulating spacer. An 11.5 mm diameter polyurethane cone is placed over the sensor to concentrate the force on the active area. A set of 17 force values were applied to the sensor using different weights in order to characterize the sensor. The range of forces applied to the sensor was between 1.2 N and 30 N, and the resistivity shown by the sensor for these forces was measured again using an Agilent 34401A digital multimeter.

V. Experimental Results and Discussion

The results of the three series of tests carried out with the setup indicated in Section 4 for TPCM, TCDIC, and CERM, respectively, are shown and discussed below. Maximum Absolute Error, MAE, of the 500 estimations made for each resistor under test is defined in each method as

$$MAE(R_x) = Maximum\left(\left|Inferred\ Value\ of\ R_x(i) - True\ Value\ of\ R_x\right|\right) \quad (28)$$
$$i \in \{1, 2, ..., 500\}$$

where i indicates the number of the measurement. The value obtained for this parameter appears in the 100 Ω to 1500 Ω resistance range in Fig. 4 for the three methods studied, corresponding to the low part of the total measured range. In this section, the X-axis of resistance values will be in a logarithmic scale in all figures. The MAE values obtained for TPCM and TCDIC increase as resistance value decreases, showing the increasing effects of quantization errors. Errors in TPCM are more significant than in the TCDIC for all resistors under test. This is due mainly to the better estimation of discharge times in the calibration resistors provided by (11). Although the MAEs for the series also increase as resistance value increases in CERM, they are always lower than those of TPCM. For the lowest resistance value in the series, 100 Ω, the error goes from 5.23 Ω in TPCM to 1.94 Ω in the TCDIC and 0.88 Ω for CERM. In contrast, TCDIC has more minor errors than CERM from a 681 Ω resistor.

The increase in MAE with the resistance value in CERM is due to the increase of $u(Ti_{xA})$ and $u(Ti_{xB})$ predicted by (21) and (23). To verify this, relative uncertainties $u(Ti_{xA})/Ti_{xA}$ and $u(Ti_{xB})/Ti_{xB}$ obtained experimentally are shown in Fig. 5(a). In this figure, these relative uncertainties are compared with their predicted theoretical values in (21) and (23). The theoretical value is constant and depends on relative uncertainty in the time measurement of R_{c2} (also obtained experimentally). A good match between experimental data and theoretical results is observed up to precisely the 681 Ω resistor. From then on, as discussed in Section 3, approximations (21) and (23) are no longer valid, and uncertainties increase rapidly. Likewise, it is confirmed that uncertainties in node A are greater than those in node B. Hence, $u(Ti_{xA})$ and $u(Ti_{xB})$ are the parameters that determine the value of T_L in (19). In our case, T_L is the experimental value of T_{xA} for the 681 Ω resistor, 616 cycles. On the other hand, Fig. 5(b) shows the results obtained for $u(R_x)$ with the CERM using only the upper equation of (19) and for the TPCM and TCDIC. It is observed how the total uncertainty of the CERM increases rapidly approximately for the same values in which $u(Ti_{xA})/Ti_{xA}$ and $u(Ti_{xB})/Ti_{xB}$ do.

In Fig. 6(a), this value of T_L has been used in CERM to compare TPCM and CERM errors over the full range of resistors under test. The green series of results corresponds to TPCM, showing the typical error profile of this method: a central zone between the two calibration resistors where the errors are the lowest in the whole series. As with any calibration method, the smallest errors should occur near the calibration resistors. In the TPCM this occurs for R_{c1} but not for R_{c2} since, in the vicinity of R_{c2}, trigger uncertainties are very high. However, it is also possible to observe in Fig. 6 that this fact does not occur for CERM (blue series) since, in the vicinity of R_{c2}, errors are reduced due to the decrease in the uncertainties using (19). On the other hand, as seen in Fig. 4, MAEs increase as resistance decreases in the low part of the range. In contrast, errors increase rapidly in the medium-high part due to trigger uncertainty, reaching a maximum of 13.1 Ω for the 16.2 kΩ resistor. In comparison, MAEs are practically constant in CERM up to the indicated value of 681 Ω. From then on, the effect of trigger uncertainty becomes more important and errors increase, although always to a lesser extent than in TPCM. CERM achieves an MAE of 6.2 Ω for a 15,010 Ω resistor (less than half that of TPCM).

Although MAEs are larger in magnitude in the medium-high part of the range than in the low zone, their relative importance is greater in the latter, as can be seen in Fig. 6(b). This figure plots Maximum Relative Error, MRE, for each resistance estimation, according to the following definition:

$$MRE(R_x) = 100 \cdot \frac{Maximum\ Absolute\ Error(R_x)}{True\ Value\ of\ R_x} \quad (29)$$

When analyzing the results in Fig. 6(b), it should be noted that CERM and TCDIC estimations are identical for $R_x \geq 681\ \Omega$. In any case, MRE in CERM, for the lower resistance value in the range, is less than five times that of TPCM and less than two times that of the TCDIC. This is important in tactile sensors, as these resistance values correspond to the typical forces in common object manipulation tasks. The MRE profile reaches minimum levels in the central part of the range in all methods and then remains approximately constant at these values, as predicted by (8). The minimum MRE values are 0.023% for CERM and 0.036% for TPCM. In the low part of the range, the MREs have a relatively constant negative slope until they reach the central minimum levels. The largest MRE are 0.88% for the CERM, 1.94% for the TCDIC, and 5.23% for the TPCM.

Another important parameter to evaluate the performance of the different methods is the maximum total time to estimate one resistance. In all methods, the maximum time occurs for the highest resistance value and consists of the sum of the three capacitor charging times plus the discharge times through R_{c1}, R_{c2}, and R_x. Charging time was selected at 2^{13} clock cycles (163.84 µs) to ensure the same final charge values in the capacitors in the circuits of Fig. 1. In accordance with the above, the maximum time needed to estimate a 16.2 kΩ resistor in TPCM is 1051.42 µs, and 1076.82 µs for the TCDIC and CERM. The difference is due to the fact that the values of C in TPCM and C_T in the TCDIC and CERM are slightly different, as discussed in Section 4. The difference in these times does not depend on the method used but on the fact that the authors cannot match the values of C and C_T (due to the commercially available values of polypropylene film capacitors). Moreover, for resistances in the low part of the range, the times will always be longer in CERM since the discharge starting through R_x and ending through R_{c2} will take longer to complete than if it were only through R_x. However, these times will always be much lower than those of resistances in the medium-high zones of the range.

Having characterized the electronic circuit used for the measurement of resistors, the next step was to connect the force sensor to the circuit. It must be remembered that forces that correspond exactly to specific resistor values cannot be exerted on the sensor. For this reason, a least squares adjustment was carried out in order to find the best function in the form α/F_x, which provides the resistance values measured in the 17 force-resistance experimental pairs. Proceeding in this way obtained α = 13,346.46 N·Ω. The regression curve, together with the experimental data, is shown in Fig. 7. This curve was used to estimate the calibration forces, F_{c1} and F_{c2}, which theoretically produce R_{c1} and R_{c2} resistor values at the sensor output. The errors presented in this way of finding F_{c1} and F_{c2} are small, especially considering that it was possible to exert forces of 6.06 N and 1.20 N in the test, as corresponding to measured resistances of 2200 Ω and 11,122 Ω, quite close to the R_{c1} and R_{c2} values used. F_{c1} = 5.75 N and F_{c2} = 1.05 N were obtained in this manner. These values allow us to use (27) to estimate the forces corresponding to the 28 resistors used in the tests. Five hundred estimations of F_x were also made for each of these resistors. The mean of these 500 estimations is compared to the force values provided by the regression curve, $\widehat{F_x}$, in Fig. 8. Furthermore, the same figure shows in blue the MRE obtained for the 500 force estimates made for each resistor using CERM. Fig. 8 also shows, in orange, the MRE for the 500 force estimates using TCDIC in conjunction with (1).

For CERM, the errors obtained practically form a monotonically increasing function. They reach the maximum for the highest applied forces, with a maximum error of 0.88% for a force of 133 N.

VI. Conclusions

Direct Interface Circuits (DICs) are an efficient alternative in reading resistive, capacitive, or inductive sensors when the aim is to obtain a digital value of the magnitude to be read. The simplest versions use only a few passive elements along with the sensor, meaning a programmable digital device attached to them can establish a magnitude-to-time-to-digital conversion. In resistive sensors, the DIC typically used in the literature is the Two-Point Calibration Method (TPCM). Together with the sensor and the programmable digital device, this circuit needs two calibration resistors and a capacitor to obtain the reading of different discharge times. TPCM has the disadvantage that errors in the estimation increase as the resistance values to be measured move away from the calibration values. A new reading method has recently been proposed, namely the Two-Capacitor Direct Interface Circuit (TCDIC), which, by including an additional capacitor, is able to reduce errors in the measurement of medium-high resistances (thousands to tens of thousands ohms). However, although the TCDIC can also decrease errors in low resistance values (hundreds of ohms), the improvement achieved in this case is small. This is a problem when reading resistive force sensors since the resistance provided by the sensor as output is inversely related to the force applied. Consequently, errors in reading high forces (several tens of Newtons) are high when using these methods. It is also a crucial issue in sensors with only low resistance values (such as various gas sensors).

This paper has presented a new measurement method, the Compact Error Reduction Method (CERM), based on the TCDIC circuit. Firstly, this takes advantage of the improvements in this method when estimating medium-high resistance values and, secondly, reduces errors in estimating low resistance values. As a proof of concept to characterize the new method, firstly, a discrete resistor reading system was built based on an FPGA as a programmable digital device. For resistance values around a few hundred ohms, CERM manages to reduce TCDIC errors by up to half, along with a fivefold reduction in TPCM errors. The discrete resistors to be measured were then replaced by a commercial force sensor, the Interlink Electronics FSR 402. The new proposed method achieves a maximum error of 0.88% in estimating the highest forces applied. This improvement comes at the expense of performing a series of additional mathematical operations to obtain the estimations. To keep the number and complexity of these operations to a minimum, CERM equations have been adapted to directly produce an output in the force domain from

time measurements. This also reduces the number of parameters to be stored in the FPGA.

REFERENCES

[1] Eventoff F.N., "ELECTRONIC PRESSURE SENSITIVE TRANSDUCER APPARATUS," 4,314,227.

[2] T. V Papakostas, J. Lima, and M. Lowe, "A Large Area Force Sensor for Smart Skin Applications," in *Proceedings of IEEE Sensors*, 2002, vol. 1, no. 2, pp. 1620–1624.

[3] M. W. Strohmayr, H. Worn, and G. Hirzinger, "The DLR artificial skin step I: Uniting sensitivity and collision tolerance," in *Proceedings - IEEE International Conference on Robotics and Automation*, 2013, pp. 1012–1018.

[4] "Interlink Electronics." [Online]. Available: https://www.interlinkelectronics.com/resistive-sensor-technology. [Accessed: 13-Mar-2021].

[5] "Tacterion." [Online]. Available: https://www.tacterion.com/. [Accessed: 12-Mar-2021].

[6] "FlexiForce Load/Force Sensors and Systems." [Online]. Available: https://www.tekscan.com/flexiforce-load-force-sensors-and-systems. [Accessed: 12-Mar-2021].

[7] J. R. Barber, "Incremental stiffness and electrical contact conductance in the contact of rough finite bodies," *Phys. Rev. E*, vol. 87, no. 1, p. 13203, 2013.

[8] L. Pastewka, N. Prodanov, B. Lorenz, M. H. Müser, M. O. Robbins, and B. N. J. Persson, "Finite-size scaling in the interfacial stiffness of rough elastic contacts," *Phys. Rev. E*, vol. 87, no. 6, p. 62809, 2013.

[9] B. Lorenz and B. N. J. Persson, "Interfacial separation between elastic solids with randomly rough surfaces: comparison of experiment with theory," *J. Phys. Condens. Matter*, vol. 21, no. 1, p. 15003, 2008.

[10] J. Castellanos-Ramos, R. Navas-González, I. Fernández, and F. Vidal-Verdú, "Insights into the Mechanical Behaviour of a Layered Flexible Tactile Sensor," *Sensors*, vol. 15, no. 10, pp. 25433–25462, Oct. 2015.

[11] J. A. Greenwood and J. B. P. Williamson, "Contact of nominally flat surfaces," *Proc. R. Soc. London. Ser. A. Math. Phys. Sci.*, vol. 295, no. 1442, pp. 300–319, 1966.

[12] J. R. Barber, "Bounds on the electrical resistance between contacting elastic rough bodies," *Proc. R. Soc. London. Ser. A Math. Phys. Eng. Sci.*, vol. 459, no. 2029, pp. 53–66, 2003.

[13] S. Nakagawa, T. Miyazaki, and H. Ishikuro, "A digital-to-resistance converter with an automatic offset calibration method for evaluating dynamic performance of resistive sensor readout circuits," *I2MTC 2020 - Int. Instrum. Meas. Technol. Conf. Proc.*, pp. 3–7, 2020.

[14] R. Gupta, V. Sreenath, and B. George, "A modified RDC with an auto-adjustable SC source enabled auto-calibration scheme," *SAS 2016 - Sensors Appl. Symp. Proc.*, pp. 94–99, 2016.

[15] N. M. Mohan, B. George, V. J. Kumar, and A. A. Dsrdc, "A Novel Dual-Slope Resistance-to-Digital Converter," *IEEE Trans. Instrum. Meas.*, vol. 59, no. 5, pp. 1013–1018, 2010.

[16] K. Elangovan, S. Dutta, A. Antony, and A. C. Sreekantan, "Performance verification of a digital interface suitable for a broad class of resistive sensors," *IEEE Sens. J.*, vol. 20, no. 23, pp. 13901–13909, 2020.

[17] S. Chavan and C. S. Anoop, "A simple direct-digitizer for Giant magneto-resistance based sensors," *Conf. Rec. - IEEE Instrum. Meas. Technol. Conf.*, vol. 2016-July, no. 1, pp. 1–5, 2016.

[18] V. Sreenath, K. Semeerali, and B. George, "A resistive sensor readout circuit with intrinsic insensitivity to circuit parameters and its evaluation," *IEEE Trans. Instrum. Meas.*, vol. 66, no. 7, pp. 1719–1721, 2017.

[19] T. Islam, A. U. Khan, and J. Akhtar, "Accuracy analysis of oscillator-based active bridge circuit for linearly converting resistance to frequency," *IMPACT 2013 - Proc. Int. Conf. Multimed. Signal Process. Commun. Technol.*, vol. 13, no. 5, pp. 305–309, 2013.

[20] A. Depari *et al.*, "Autobalancing Analog Front End for Full-Range Differential Capacitive Sensing," *IEEE Trans. Instrum. Meas.*, vol. 67, no. 4, pp. 885–893, 2018.

[21] Ó. Oballe-Peinado, J. A. Hidalgo-López, J. A. Sánchez-Durán, J. Castellanos-Ramos, and F. Vidal-Verdú, "Architecture of a tactile sensor suite for artificial hands based on FPGAs," in *Proceedings of the IEEE RAS and EMBS International Conference on Biomedical Robotics and Biomechatronics*, 2012.

[22] E. Sifuentes, R. González-Landaeta, J. Cota-Ruiz, and F. Reverter, "Microcontroller-Based Seat Occupancy Detection and Classification," *Proceedings*, vol. 2, no. 13, p. 1040, 2018.

[23] F. Reverter, "Interfacing sensors to microcontrollers: a direct approach," *Smart Sensors MEMs*, pp. 23–55, Jan. 2018.

[24] A. Webjörn, "Simple A/D for MCUs without built-in A/D converters, AN477," Milton Keynes, UK, 1993.

[25] D. Sherman, "Measure Resistance and Capacitance without an A/D, AN449," Sunnyvale, CA, 1993.

[26] Z. Kokolanski, C. Gavrovski, V. Dimcev, and M. Makraduli, "Hardware Techniques for Improving the Calibration Performance of Direct Resistive Sensor-to-Microcontroller Interface," *Metrol. Meas. Syst.*, vol. 20, no. 4, pp. 529–542, Dec. 2013.

[27] Z. Czaja, "Time-domain measurement methods for R, L and C sensors based on a versatile direct sensor-to-microcontroller interface circuit," *Sensors Actuators A Phys.*, vol. 274, pp. 199–210, May 2018.

[28] J. E. Gaitán-Pitre, M. Gasulla, and R. Pallàs-Areny, "Analysis of a direct interface circuit for capacitive sensors," *IEEE Trans. Instrum. Meas.*, vol. 58, no. 9, pp. 2931–2937, 2010.

[29] Z. Kokolanski, F. Reverter Cubarsí, C. Gavrovski, and V. Dimcev, "Improving the resolution in direct inductive sensor-to-microcontroller interface," *Annu. J. Electron.*, pp. 135–138, 2015.

[30] Z. Czaja, "A microcontroller system for measurement of three independent components in impedance sensors using a single square pulse," *Sensors Actuators, A Phys.*, vol. 173, no. 1, pp. 284–292, 2012.

[31] A. Anarghya, S. S. Rao, M. A. Herbert, P. Navin Karanth, and N. Rao, "Investigation of errors in microcontroller interface circuit for mutual inductance sensor," *Eng. Sci. Technol. an Int. J.*, vol. 22, no. 2, pp. 578–591, Apr. 2019.

[32] L. Dutta, A. Hazarika, and M. Bhuyan, "Nonlinearity compensation of DIC-based multi-sensor measurement," *Measurement*, vol. 126, pp. 13–21, Oct. 2018.

[33] J. A. Hidalgo-Lopez, J. A. Sanchez-Duran, and O. Oballe-Peinado, "Method to Reduce Quantization Error in Direct Interface Circuits for Resistive Sensors," *IEEE Sens. J.*, vol. XX, no. XX, pp. 1–1, 2020.

[34] J. A. Hidalgo-López, Ó. Oballe-Peinado, J. Castellanos-Ramos, and J. A. Sánchez-Durán, "Two-capacitor direct interface circuit for resistive sensor measurements," *Sensors*, vol. 21, no. 4, pp. 1–17, Feb. 2021.

[35] F. Reverter, M. Gasulla, R. Pallas-Areny, and R. Pallàs-Areny, "Analysis of Power-Supply Interference Effects on Direct Sensor-to-Microcontroller Interfaces," *IEEE Trans. Instrum. Meas.*, vol. 56, no. 1, pp. 171–177, 2007.

[36] F. Reverter and R. Pallàs-Areny, "Effective number of resolution bits in direct sensor-to-microcontroller interfaces," *Meas. Sci. Technol.*, vol. 15, no. 10, pp. 2157–2162, Oct. 2004.

[37] Xilinx Inc., "Spartan-6 FPGA Data Sheet," *January*, vol. 162, pp. 1–89, 2015.

[38] J. Castellanos-Ramos *et al.*, "Adding proximity sensing capability to tactile array based on off-the-shelf FSR and PSoC," *IEEE Trans. Instrum. Meas.*, vol. 69, no. 7, pp. 4238–4250, 2020.

This article has been accepted for publication in IEEE Sensors Journal. This is the author's version which has not been fully edited and content may change prior to final publication. Citation information: DOI 10.1109/JSEN.2021.3107589

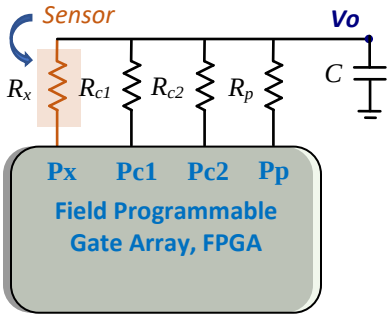

(a)

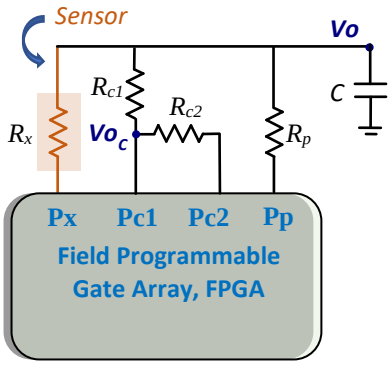

(b)

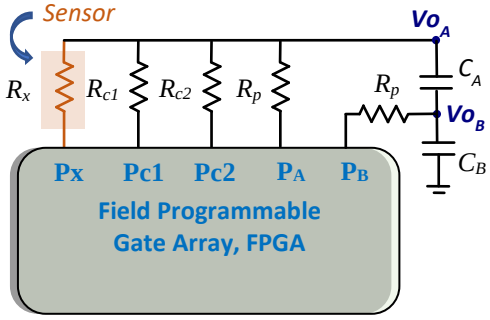

(c)

Fig. 1. Different types of DICs presented in the literature: (a) Two-Point Calibration Method (TPCM); (b) Quantization Error Reduction Method (QERM), to reduce quantization uncertainty; (c) Two-Capacitor DIC (TCDIC), to reduce trigger uncertainty. This circuit is also used by the new R_x estimation method proposed by the authors.

This article has been accepted for publication in IEEE Sensors Journal. This is the author's version which has not been fully edited and content may change prior to final publication. Citation information: DOI 10.1109/JSEN.2021.3107589

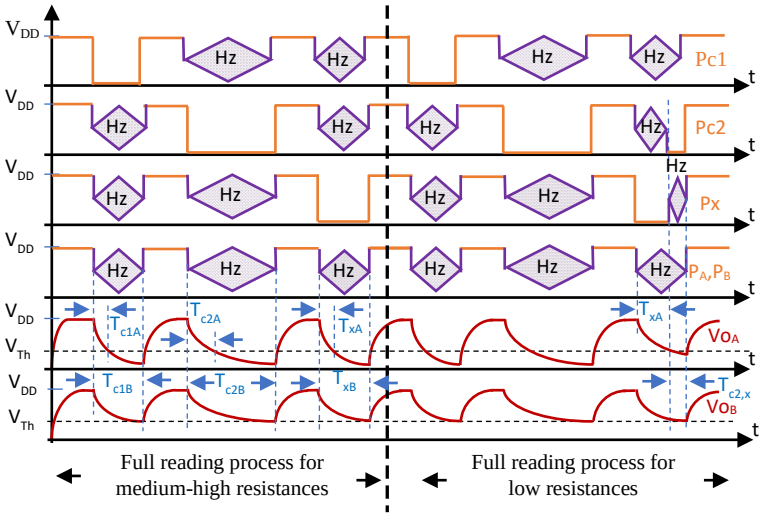

Fig. 2. Waveforms for the pins of the PDD and voltages V_{oA} and V_{oB} of the CERM circuit for the two possible situations: on the left side, when R_x has medium-high values and, on the right side, when R_x has low values.

This article has been accepted for publication in IEEE Sensors Journal. This is the author's version which has not been fully edited and content may change prior to final publication. Citation information: DOI 10.1109/JSEN.2021.3107589

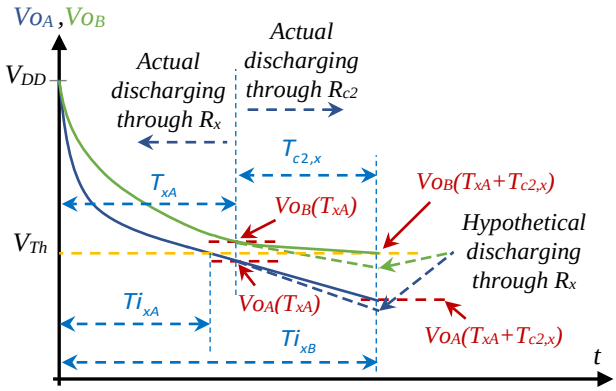

(a)

Fig. 3. Discharge process in the Compact Error Reduction Method for low resistances. The discharge occurs first through R_x and continues through R_{c2}. Thus, the circuit only measures times T_{xA} and $T_{c2,x}$. Times Ti_{xA} and Ti_{xB} are inferred from them.

This article has been accepted for publication in IEEE Sensors Journal. This is the author's version which has not been fully edited and content may change prior to final publication. Citation information: DOI 10.1109/JSEN.2021.3107589

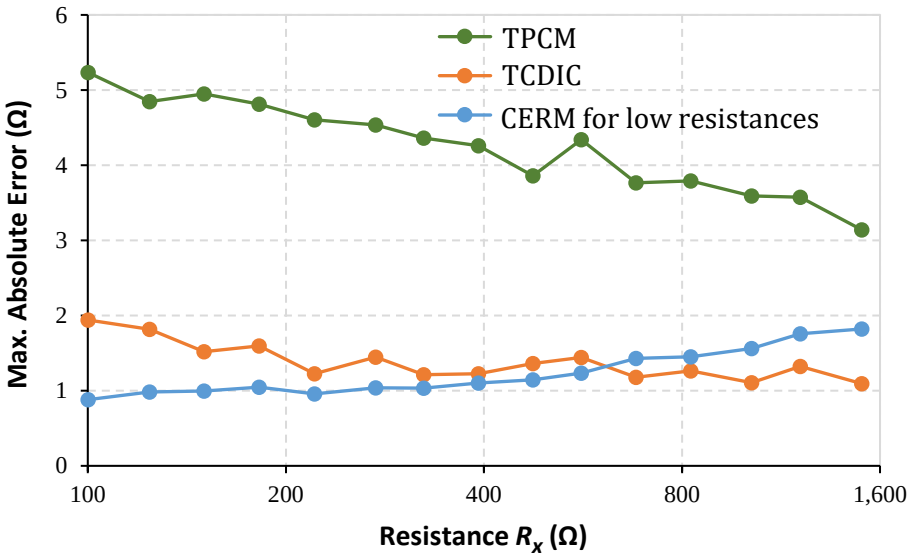

Fig. 4. Maximum Absolute Error (MAE) in estimating R_x, for low resistances only, using the Two-Point Calibration Method (TPCM) (green series), the Two-Capacitor DIC (TCDIC) (orange series), and equation (18) corresponding to the Compact Error Reduction Method (CERM) (blue series) for the case $T_{xA} < T_L$. The X-axis, in log2 scale, shows the resistors used.

This article has been accepted for publication in IEEE Sensors Journal. This is the author's version which has not been fully edited and content may change prior to final publication. Citation information: DOI 10.1109/JSEN.2021.3107589

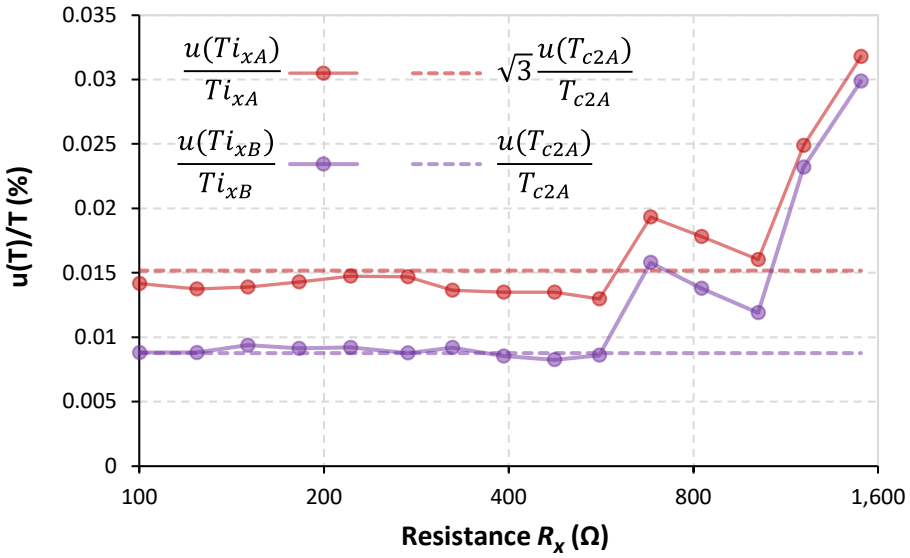

(a)

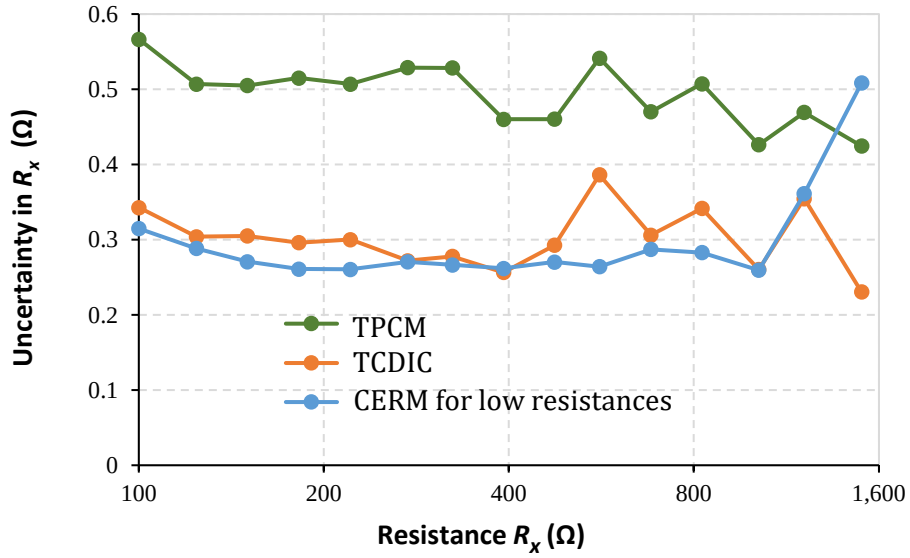

(b)

Fig. 5. (a) Relative uncertainties in measurement times Ti_{xA} and Ti_{xB}. The results are compared with their theoretical values for low resistances, shown by the dashed lines. (b) Uncertainty in the estimation of R_x by the three methods. The two figures show that $u(R_x)$ increases strongly in the CERM, using only the upper equation of (19), for the same resistance values as in the case of $u(Ti_{xA})/ Ti_{xA}$ and $u(Ti_{xB})/ Ti_{xB}$.

This article has been accepted for publication in IEEE Sensors Journal. This is the author's version which has not been fully edited and content may change prior to final publication. Citation information: DOI 10.1109/JSEN.2021.3107589

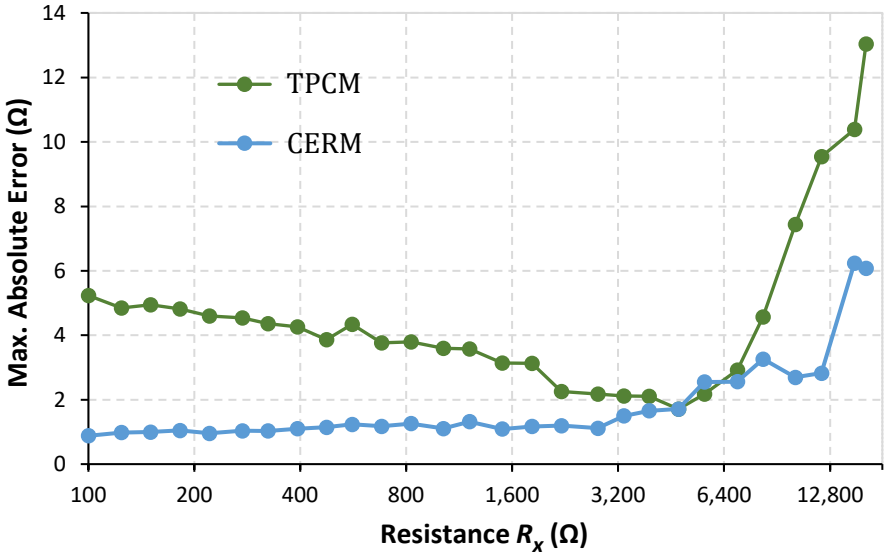

(a)

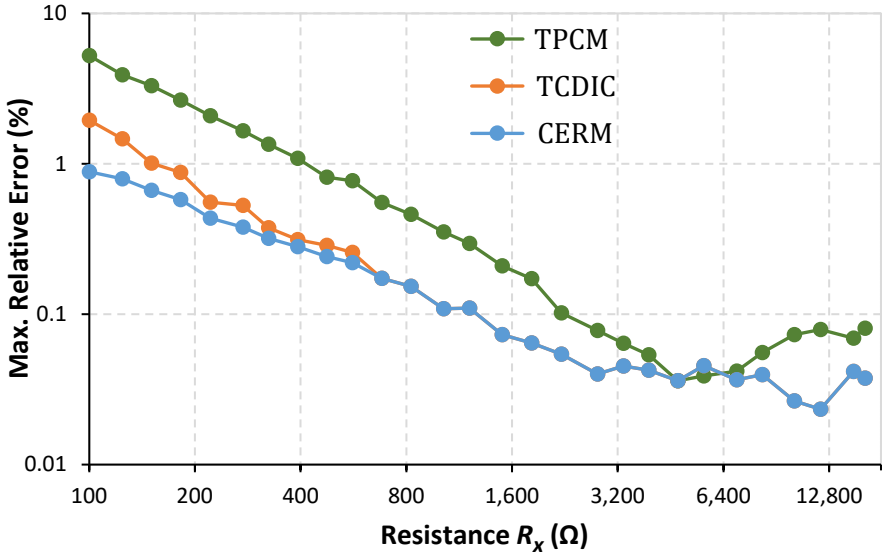

(b)

Fig. 6. (a) Maximum Absolute Error (MAE) in TPCM (green series) and in CERM (blue series) with T_L corresponding to a 681 Ω resistor (616 clock cycles). (b) Maximum Relative Error (MRE) in TPCM, CERM, and in the TCDIC. Again, CERM results are shown for T_L = 616 clock cycles.

This article has been accepted for publication in IEEE Sensors Journal. This is the author's version which has not been fully edited and content may change prior to final publication. Citation information: DOI 10.1109/JSEN.2021.3107589

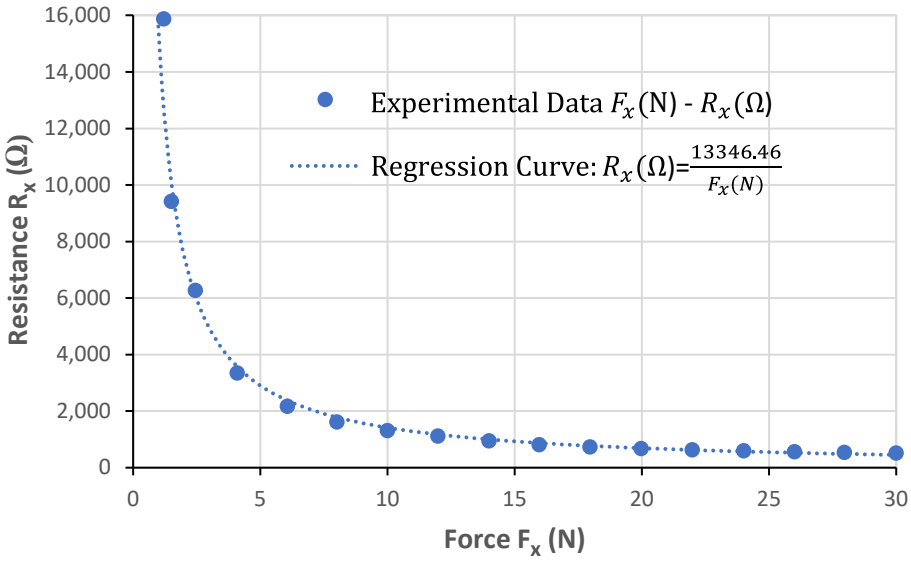

Fig. 7. Comparison between the experimental pairs *Applied Force (F_x)* - *Measured Resistance (R_x)* and the regression curve obtained from these experimental data.

This article has been accepted for publication in IEEE Sensors Journal. This is the author's version which has not been fully edited and content may change prior to final publication. Citation information: DOI 10.1109/JSEN.2021.3107589

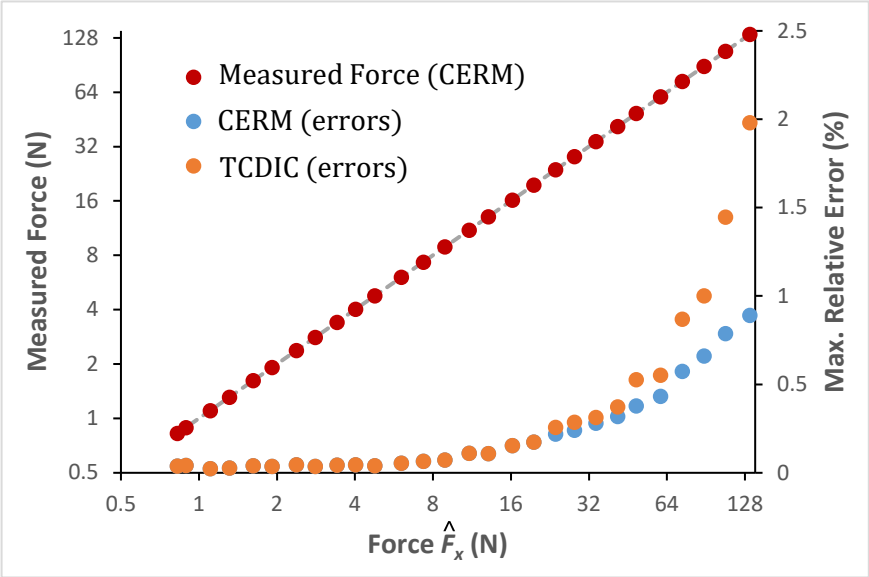

Fig. 8. Measured Force obtained using CERM, equation (27), versus theoretical force applied to the sensor, $\widehat{F_x}$, obtained from the regression curve for each of the 28 resistors being tested (red). Blue and Orange show the MRE of the 500 force estimates made for each resistor using CERM and TCDIC, respectively.